

1 **GPS displacement dataset for study of elastic surface mass**
2 **variations**

3
4 Athina Peidou¹, Donald Argus¹, Felix Landerer¹, David Wiese¹ and Matthias Ellmer¹
5 Jet Propulsion Laboratory, California Institute of Technology, Pasadena, CA, USA, 2023

6
7 *Correspondence to:* Athina Peidou (athina.peidou@jpl.nasa.gov)

8 © 2023. California Institute of Technology. Government sponsorship acknowledged.

9 **Abstract**

10 Quantification of uncertainty in surface mass change signals derived from GPS measurements poses
11 challenges, especially when dealing with large data sets with continental or global coverage. We present a
12 new GPS station displacement data set that reflect surface mass load signals and their uncertainties. We
13 assess the structure and quantify the uncertainty of vertical land displacement derived from 3045 GPS
14 stations distributed across the continental US. Monthly means of daily positions are available for 15
15 years. We list the required corrections to isolate surface mass signals in GPS estimates and screen the data
16 using GRACE(-FO) as external validation. Evaluation of GPS timeseries is a critical step, which
17 identifies a) corrections that were missed; b) sites that contain non-elastic signals (e.g., close to aquifers);
18 and c) sites affected by background modelling errors (e.g., errors in the glacial isostatic model). Finally,
19 we quantify uncertainty of GPS vertical displacement estimates through stochastic modeling and
20 quantification of spatially correlated errors. Our aim is to assign weights to GPS estimates of vertical
21 displacements, which will be used in a joint solution with GRACE(-FO). We prescribe white, colored and
22 spatially correlated noise. To quantify spatially correlated noise, we build on the common mode imaging
23 approach adding a geophysical constraint (i.e., surface hydrology) to derive an error estimate for the
24 surface mass signal. We study the uncertainty of the GPS displacements, derived using each technique
25 and find that three techniques exhibit an average noise level between 2-3 mm: white noise, flicker noise,
26 and RMS of residuals about a seasonality and trend fit. Prescribing random walk noise increases the error
27 level such that half of the stations have noise > 4 mm, which is systematic with the noise level derived
28 through modeling of spatial correlated noise. The new data set is suitable for use in a future joint solution
29 with GRACE(-FO)-like observations.
30

31
32 Keywords: GPS uncertainty | elastic displacement | GRACE-FO | surface mass change

33
34 **1. Introduction**

35
36 For more than two decades, the Gravity Recovery and Climate Experiment (GRACE) space gravity
37 mission and its nearly identical successor mission, GRACE-Follow on (GRACE-FO), have provided
38 mass change estimates through tracking the time-variable part of the Earth’s gravity field (Landerer et al.,
39 2020). Mass change products are typically given on a monthly basis and have been used to study a variety

Deleted: land

Deleted: (VLD)

Deleted: VLD

Deleted: vertical land

44 of critical climate-related factors (Tapley et al., 2019), such as sea level rise (Frederikse et al., 2020); ice
 45 mass change (Velicogna et al., 2020); prolonged drought periods (Thomas et al., 2014) and regional flood
 46 potentials (Reager et al., 2014). The measurement geometry of GRACE(-FO) limits the study of
 47 geophysical processes to spatial scales of ~300 km and larger, for monthly timespans. Recent community
 48 reports (Pail et al., 2015, Wiese et al., 2022) have highlighted the utility and need of mass change
 49 observations at improved spatial resolutions to address a number of science and applications objectives.
 50 Examples include closure of the terrestrial water budget for small to medium sized river basins, and
 51 separation of surface mass balance from ice dynamic processes at the scale of individual outlet glacier
 52 systems.

53 The spatial resolution of gravity maps derived from satellite measurements is limited by sampling at
 54 altitude. Fusion with external geodetic data sources, however, can improve spatial resolution over what
 55 can be achieved only with satellite gravimetry. GPS position timeseries have been used widely to study
 56 the elastic response of Earth's surface to mass loading (e.g., Argus et al., 2017; Fu and Freymueller,
 57 2012) and can provide information at short wavelengths (~100km) (Argus et al., 2021). Solid Earth
 58 responds elastically to changes in the surface load of water, snow, ice, and atmosphere. When the Earth's
 59 surface is loaded with mass (e.g., snow and water) it subsides; and when mass loads are removed the
 60 surface rises. Thus, the Earth's response follows the water cycles such that: precipitation and snow
 61 accumulation cause subsidence of the surface and snow melt, evaporation and water run off allow the
 62 Earth's surface to bounce back (uplift). Focus is typically placed on the radial direction (vertical), due to
 63 the rapid decrease of vertical displacement with the distance from a surface load (Argus et al., 2017),
 64 which leads to high fidelity estimates in the space domain. Note that across certain geological formations
 65 such as aquifers, subduction zones and regions with volcanic activity surface loading is mixed with other
 66 solid Earth/geophysical processes making it difficult to isolate the elastic component. Therefore, GPS
 67 sites located at the vicinity of such formations are omitted.

68 GPS displacements between two epochs have many different signals embedded in them: i.e., those related
 69 to atmospheric and oceanic loading, solid Earth phenomena such as tectonics, glacial isostatic adjustment,
 70 and others related to surface mass changes. With the proper treatment (see Sec.2) GPS stations can
 71 capture local surface mass changes. We are interested in isolating the signals that reflect the Earth's
 72 elastic response to mass variations, thus we apply a set of corrections to GPS vertical displacement
 73 estimates, and then we screen the data for outliers or potential errors. The data screening process checks
 74 for consistency between GPS and GRACE(-FO) vertical displacement estimates (similar analysis has
 75 been performed by Yin et al., 2020; Blewitt et al., 2001; van Dam et al., 2001; Becker and Bevis, 2004;
 76 Davis, 2004; Tregoning et al., 2009; Tsai, 2011 and Chew et al., 2014) and identifies outliers that
 77 statistical tests fail to pick up (He et al., 2018).

78 The last step is to estimate uncertainty in the screened data set. Since our purpose is to isolate surface
 79 mass load signals, we define *error* as any vertical displacement signal that does not reflect an elastic
 80 surface mass load. The reported uncertainty of a measurement reflects the sum of all error sources to the
 81 measurement, and is the final product of this study. Error correlation (temporal and spatial) and the
 82 deficiency of stochastic noise models to describe the error realistically are the main challenges in this
 83 uncertainty quantification task.

84 Error sources include errors driven by satellite antenna phase centre offsets (Haines et al., 2004;
 85 Santamaria-Gomez et al., 2012); atmospheric pressure models (Kumar et al., 2020); non-tidal ocean
 86 loading (Jiang et al., 2013); satellite orbits (Ray et al., 2008; Amiri-Simkooei, 2013); earth orientation

Deleted: subside

Deleted: land

Deleted: (VLD)

Deleted: from further analyses

Deleted: VLDs (i.e., displacement

Deleted:)

Deleted: (GIA),

Deleted: VLD

Deleted: VLD

Deleted: VLD

Deleted: ,

98 parameters (Rodriguez-Solano et al., 2014); and tectonic trends and post-seismic relaxation after
 99 earthquake activity (Ji and Herring, 2013; Crowell et al., 2016).
 100 Many of the error sources are “common mode” (also called common model noise, Tian and Shen 2016).
 101 Wdowski et al. (1997) first defined common mode error to be a series of rigid-body translations that
 102 reflect an error in the position of all geodetic sites in an area relative to an absolute reference frame; by
 103 removing the mean position (or stack) of all sites in an area, scientists recover more accurate estimates of
 104 relative position contained in the data. Dong et al. (2006) and Serpelloni et al. (2013) defined common
 105 model error in a more sophisticated manner using principal or independent component analysis such that
 106 they remove spatially correlated, temporally incoherent error. Independent is different than principal
 107 component analysis in that it finds the maximum independence of the components instead of minimum
 108 correlation (Milliner et al., 2019; Liu et al., 2015). Common mode error may include both error (such as
 109 that associated with error in satellite orbits) and signal (such as the seasonal oscillation of elastic vertical
 110 displacement in elastic response to seasonal fluctuations in mass between the hemispheres) (Sun et al.
 111 2016).
 112 Considering the increased number of GPS stations and the limitations posed by the existing
 113 methodologies, Kreemer and Blewitt (2021) used a robust methodology to estimate the common spatial
 114 components of GPS residuals (i.e., the remaining signals of a time-series after subtraction of a trajectory
 115 model). A trajectory model is a model consisting of an offset, a rate, and a sinusoid with a period of 1
 116 year (Bevis and Brown, 2014).
 117 The so-called common mode component (CMC) imaging technique was originally introduced by Tian
 118 and Shen (2016) and quantifies the spatial correlation of the residuals (position or vertical displacement
 119 time-series anomaly with respect to a trajectory model) of unequal-length time-series using information
 120 from neighbor stations. It is important to note that CMC reflects both spatially correlated noise and
 121 spatially correlated signals, including elastic displacements, that a trajectory model fails to describe.
 122 Spectral analysis of the residuals (with respect to a trajectory model, see Eq.2) is an alternative way to
 123 estimate the noise level of vertical displacement series for each GPS station. The spectrum of the
 124 residuals can be approximated by white or colored noise (flicker, random walk, power law approximation,
 125 generalized gauss markov etc.), or by a combination of white and colored noise (Williams et al., 2004;
 126 Bos et al., 2008; Klos et al., 2014). A summary of the different noise models and their power distribution
 127 can be found in He et al. (2018). Several standard GPS time series analysis packages are available to
 128 perform such an analysis, e.g., the Create and Analyze Time Series (CATS) (Williams, 2008) and Hector
 129 (Bos et al. 2013). Various studies in the past suggested that the residuals are better described by a
 130 combination of white and flicker noise (see e.g., Klos et al., 2014; Argus et al., 2017), with the latter
 131 contributing the most (Argus and Peltier, 2010). Recently, Argus et al. (2022), showed that the longer the
 132 timeseries the more the spectrum of GPS residuals converges with the noise model of random walk.
 133
 134 Here, we outline a comprehensive framework for processing large data sets (continental and/or global) of
 135 GPS timeseries, to derive estimates that only reflect surface mass signals, for use in a joint inversion with
 136 GRACE(-FO) measurements. Originally, we layout the corrections required to capture local surface mass
 137 changes (Section 2.1). Our interest is to make the process as automated as possible, thus we set a number
 138 of evaluation metrics to detect outliers among all candidate (for the joint inversion) sites. Stations flagged
 139 as outliers are further evaluated for extra corrections (e.g., offsets; poor site maintenance etc.). Finally, we
 140 assign weights to each GPS vertical displacement record. We test the most popular methodologies to
 141 quantify the error, considering time-correlation, spatial-correlation and/or white noise (Section 3). Note

- Deleted: Most
- Deleted: these errors
- Deleted: also spatially coherent, and their sum is usually referred to as
- Deleted: -
- Deleted: (CMN) (Kreemer and Blewitt; 2021). Mitigation of CMN is usually done by means of spatial filtering (
- Deleted:), a technique that needs
- Deleted: applied with caution, due to the assumptions made when applying
- Deleted: spatial filter (see e.g., Williams, 2004; Tian and Shen 2016). Recent developments of spatial filtering algorithms include
- Deleted: component analysis (PCA)
- Deleted: (ICA). PCA decomposes residual time-series (relative to a deterministic model) into various principal/independent components based on their variance and identifies the components that reflect CMN (Serpelloni et al., 2013; Li and Shen,
- Moved down [1]: 2018).
- Deleted: ICA
- Deleted: PCA
- Deleted: One of the main limitations
- Deleted: PCA/ICA is their susceptibility to dismiss CMN reflected in a relatively small number of stations. Therefore, in many occasions a subset of stations is studied independently (Wu et al., 2019
- Deleted: developed
- Deleted: deterministic
- Deleted: VLD
- Deleted: deterministic
- Deleted: deterministic
- Deleted: deterministic
- Deleted: VLD
- Deleted: CATS
- Deleted: In this contribution
- Deleted: VLD
- Deleted: VLD
- Deleted: VLD

181 that for spatially correlated noise the commonly used PCA/ICA is not as applicable to our use case,
182 because our data set extends over very large spatial areas (continental). CMC imaging (Kreemer and
183 Blewitt; 2021) fits our needs better. We build on the existing CMC algorithm to remove hydrology
184 signals from the error estimate by deriving surface loading signals from a hydrology model and removing
185 them from the GPS up displacements (see Section 3 for more details). The final product is a new data set
186 with GPS vertical displacement estimates that reflect elastic mass variations and their uncertainties.
187

Deleted: 2020
Deleted: overcome CMC's limitation of include spatially correlated...
Deleted: in
Deleted: .
Deleted: VLD

188 2. GPS data processing and screening

189

190 2.1 Isolating surface mass loading fingerprint from GPS vertical displacements

191 We analyze positions of 3054 GPS sites as a function of time from 2006 to 2021 estimated by scientists at
192 the Nevada Geodetic Laboratory (NGL) (Blewitt et al. 2018). Technologists at Jet Propulsion Laboratory
193 (JPL) first estimate satellite orbits, satellite clocks, and positions for a core set of roughly 50 sites on
194 Earth's surface (Bertiger et al. 2020). NGL uses JPL's clock and orbit products and performs point
195 positioning to a total of about 18,500 GPS sites distributed across the world. Following the International
196 Earth Rotation Standards (IERS) (Petit and Luzum, 2012) NGL's positions are corrected for solid Earth,
197 ocean, and pole tides. NGL's positions in International Terrestrial Reference Frame 2014 (ITRF2014)
198 (Altamimi et al. 2016) are more accurate than NGL's previous estimates of positions in ITRF2008. NGL
199 estimates GPS wet tropospheric delays each day using the ECMWF weather model (Simmons et al. 2007)
200 and the VMF1 tropospheric mapping function (Boehm et al. 2006). We analyze GPS position-time series
201 following Argus et al. (2010, 2017, 2021). To isolate the part of GPS displacements reflecting solid
202 Earth's elastic response, we:

Deleted: VLD

Moved (insertion) [1]

Deleted: ¶
The 3054 GPS position time-series used in this study are a product of Jet Propulsion Laboratory (JPL) (Bertiger et al., 2020) and Nevada Geodetic Laboratory reprocessed GPS solutions (Blewitt et al., 2018). GPS satellite orbits, clocks, and core site positions are estimated consistently using the latest techniques and GipsyX software (Bertiger et al., 2020). Displacement signals driven by solid earth, oceanic and pole tides are corrected according to International Earth Rotation Service (IERS) standards. ¶
We process the GPS series similar to Argus et al. (2017; 2022), that is, we correct for atmospheric loading signals using the ECMWF weather model (Simmons et al., 2007) and for GIA, using the ICE-6G_D model (Peltier et al., 2018). GIA modelling errors affect GPS and GRACE(-FO) VLD predictions in opposite sense. Overestimation of GIA translates to subsidence when we correct GPS. The same overestimation predicts too much mass gain and shows as water loss when we correct GRACE(-FO), which eventually translates to land uplift. The same analogy applies to underestimation of GIA, which is mapped as uplift on GPS and as subsidence on GRACE(-FO) VLD predictions. ¶
Estimates prior to or after a significant earthquake event, or biased by a significant post-seismic transient are discarded. Stations with non-elastic response (e.g., porous) located at aquifers, volcanically active regions and oil extraction sites are also removed from the data record (see Argus et al. (2017) for details). An interseismic strain accumulation correction across the Cascadia is also applied (Argus et al., 2021). The model (Li et al. 2018) consists of both elastic and viscous components (2/3 elastic and 1/3 viscous). ¶
All estimates are given in the International Terrestrial Reference Frame 2014 (Altamimi et al., 2016). Finally, we solve for and remove an offset (Argus et al., 2010) if an estimated offset is greater than 8 mm in the radial direction. In most cases, estimating the offset reduces the root mean square dispersion (in mm) of the position estimates about a fit of the position, velocity and sinusoid with an annual frequency, by more than 5 percent. Daily solutions are averaged into monthly means, and are available for different durations over a span of fifteen years starting from 2006. ¶
To compare GPS with GRACE(-FO) VLD estimates we reference all VLD data

203
204 a. Construct time series of elastic displacement uninterrupted by offsets due to antenna substitutions or
205 earthquakes that pass through a specific reference time (such as Jan 1, 2014) by eliminating data before
206 and /or after an offset.

207
208 b. Identify and omit GPS sites recording primarily i. poreoleastic response to change in groundwater, ii.
209 strong volcanic fluctuations, and iii. postseismic transients following Argus et al. (2014, 2017, 2022). In
210 the west U.S., GPS sites responding to groundwater change have maximum height around April when
211 water is maximum, subside in the long term faster than 1.8 mm/yr, exhibit strong transients, and/or are
212 located in known aquifers (Argus et al. 2014). Volcanic activity is readily identified by Interferometric
213 Synthetic Aperture Radar (InSAR) and GPS observations of strong transients and anomalous sustained
214 uplift or subsidence (Argus et al. 2014, Hammond et al. 2016).

215
216 c. Remove non-tidal atmospheric (NTAL) and non-tidal oceanic (NTOL) mass loading by interpolating
217 global grids of elastic displacements calculated by the German Center for Geoscience (GFZ) (Dill
218 Dobslaw, 2013) following the method of Martens et al. (2020).

219
220 d. Remove glacial isostatic adjustment as predicted by model ICE-6G_D (VM5a) (Peltier et al. 2015,
221 2018; Argus et al. 2014).

222
223 e. Remove interseismic strain accumulation associated with locking of the Cascadia subduction zone
224 using an upgrade of the model of Wang et al. (2018). The model is superposition of 2/3 of the elastic and

1/3 of the viscoelastic model of Wang et al. (2018). We communicated with Li Wang and his team at National Resources Canada, that the Wang et al. (2018) model does not fit the available GPS data; they have produced an interim model using our input that more nearly fits the GPS data.

f. Average the daily estimates of GPS position into monthly means centered at the center of each month from January 2006 to June 2021.

To compare GPS with GRACE(-FO) vertical displacement estimates we reference the series to the epoch with the most GPS site records, which is September 2012. This process results in an 11% loss of stations (i.e., no available measurement on 09/2012). Similar to Yin et al. (2020), detrended monthly estimates of each station that are larger than 3σ relative to the mean of the time-series are considered outliers and removed from the data set. Statistical outliers comprise $\sim 0.5\%$ of the records. 2705 (or 88.8%) of GPS stations remain after the choice of reference epoch, the 3σ test and the removal of sites with non-elastic loading response. The distribution of sites is denser along the East and West coasts, and fairly sparse in the central-north US (Fig.1). Series of two arbitrary stations (hivi and njwt) located at the West and East coast respectively, are shown in Fig. 1. The response of the Earth on the extensive drought period in California between 2011.5-2015.5 is captured in the uplift trend mapped by hivi station (Fig.1, top right panel; dashed blue line).

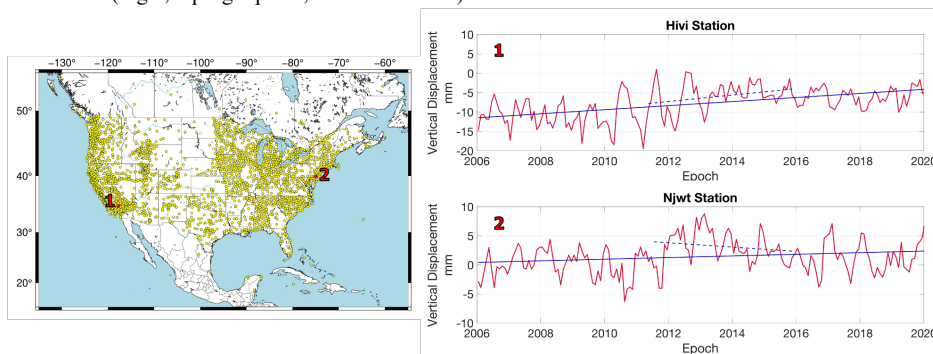


Figure 1: Left panel) Map of study area. GPS stations are shown in yellow; Right panel) Vertical displacement timeseries of two random stations (red line). Solid blue line denotes the overall trend of the timeseries and dashed blue line the trend between (2011.5-2015.5). Note the significant uplift of the hivi station located in southern California.

2.2 External validation data sets - Time-variable gravity field

We compare GPS observations of vertical displacement against GRACE(-FO) estimates of solid Earth's elastic vertical displacement from terrestrial water, snow, and ice. To compare to GRACE(-FO), we analyze JPL's three-degree mascon solution (Release 6, Watkins et al. 2015, Wiese et al. 2016). The effect of glacial isostatic adjustment is removed from GRACE(-FO) products using ICE-6G_D model estimates (Peltier et al., 2017). The geocentre motion (degree 1) coefficient is using the technique of Sun et al. (2016) (Technical Note 13). Values of C20 (Earth's oblateness) and C30 (for months after Aug 2016) are substituted with SLR data (Loomis et al., 2019). We

Deleted: employ

Deleted: mascon solutions developed at the Jet Propulsion Laboratory that resolve mass changes using 3

Deleted: spherical cap basis functions (

Deleted: ,

Deleted: ; Watkins et al., 2015) as a validation tool for the GPS data.

Deleted: postglacial rebound

Deleted: replaced with

Deleted: estimated coefficient from

Deleted:), using TN-

Deleted: . The Earth's

Deleted: coefficient (C20) is replaced by an estimate derived from Satellite Laser Ranging observations for all months...

Deleted:), as is the C30 coefficient for all months after August 2016, due to only having a single functioning accelerometer. GPS position timeseries

327 calculate solid Earth's elastic response by using the loading Love number of the Preliminary Reference
 328 Earth Model (Wang et al.; 2012).
 329 Estimates of GPS positions in ITRF2014 (Altamimi et al. 2016) are relative to center of mass (CM) in the
 330 long term but relative to center of figure (CF) in the seasons (because ITRF2014 does not allow there to
 331 be seasonal oscillations of CM). We therefore remove the long-term rate of CM relative to CF to
 332 transform the GRACE estimates in the long term from CF to CM (but do not remove seasonal oscillations
 333 of CM relative to CF so as to preserve the ITRF seasonal frame relative to CF). The annual signal of the
 334 geocenter (as realized by ITRF 2014) projected on the up component in north America on average
 335 explains 3% of the GPS vertical displacement signal and can explain up to 20% for certain sites.
 336 GRACE(-FO) vertical displacement monthly estimates are derived as follows (e.g., Davis et al., 2004):

$$U(\phi, \lambda) = a \sum_{l,m} \left(\frac{h_l^E}{1 + k_l^E} \right) P_{lm}(\sin\lambda) \times [C_{lm} \cos m\phi + S_{lm} \sin m\phi] \quad (1)$$

338
 339 Where, U is the estimate of vertical displacement, a denotes the Earth's radius, ϕ, λ denote the latitude
 340 and longitude, respectively; P_{lm} are the associated Legendre polynomials, and are the elastic and vertical
 341 Love numbers (Wang et al., 2012), respectively, and C and S are the spherical harmonic coefficients
 342 derived from GRACE(-FO) monthly solutions with respect to degree l and order m . JPL releases gridded
 343 mascon fields, to derive spherical harmonics (C and S in Eq. 1). We transform fields of equivalent water
 344 height to normalized harmonic coefficients using the inverse of Eq. 9 in Wahr et al. (1998). Like GPS,
 345 we subtract the GRACE(-FO) vertical displacement field of September 2012 from each monthly field to
 346 establish a common reference basis. GRACE(-FO) fields are estimated at a 0.5-degree spatial resolution
 347 (ϕ, λ in Eq.1). Thus, we extract GRACE(-FO) estimates at the station level by interpolating bilinearly the
 348 vertical displacement from the nearest 0.5-degree grid point neighbors to the station's location.

350 2.3 Screening metrics

351
 352 GPS vertical displacement estimates are evaluated against the ones derived from GRACE(-FO), to assist
 353 in identifying outliers or further corrections that may be needed. We employ a number of different metrics
 354 to evaluate the agreement between the two data sets, and to determine whether to include it in the joint
 355 solution or not. Similar to Yin et al. (2020) we quantify correlation and variance reduction between GPS
 356 and GRACE(-FO) vertical displacements. The structure of surface mass periodic signals (e.g., annual
 357 cycles, trends) as picked up by the two measurement techniques, also entails critical information
 358 regarding mismodelled offsets, and is evaluated as well.
 359 This process flags sites that need correction and corroborates joint inversion's hypothesis (Argus et al.,
 360 2021), that a basic level of agreement is needed for the GPS data to be used to infer surface mass change.

362 *Correlation*

363
 364 First, we specify the level of agreement between the data sets by estimating the Pearson correlation
 365 coefficient between GPS and GRACE(-FO) timeseries. On average the correlation is 62%, but stations
 366 located on the West coast exhibit an agreement higher than 80%, which in most cases is driven by the
 367 larger annual signal amplitude there. A more detailed look into the correlation metric is performed to

Deleted: include the linear trend of the geocentre motion (i.e., the linear trend of the ITRF14

Deleted: is approximately zero, Altamimi et al. (2014)), as opposed to GRACE(-FO), thus we remove it from GRACE(-FO)...

Deleted: geocentre

Deleted: ITRF14

Deleted: can explain up to 20% of the GPS VLD signal.

Deleted: VLD

Deleted: PREM;

Deleted: Similar to GPS, we subtract September 2012 values from the rest of the series for a common reference basis

Deleted: VLD

Deleted: VLDs.

Deleted: platforms

Deleted: ¶

Deleted: &

Deleted: VLD

386 evaluate the agreement of GPS/GRACE(-FO) in retrieving the seasonal cycle amplitude in different
387 watersheds. We fit and remove a [trajectory](#) model $y(t)$:
388

$$y(t) = a + bt + A\sin(2\pi t) + B\cos(2\pi t), \quad (2)$$

389
390 with a being the intercept; b being the trend and A and B being the [amplitudes of the sine](#) and [cosine](#)
391 [components](#) of a periodic function.

392
393 We classify stations in watersheds and plot the GPS-GRACE(-FO) correlation coefficient (R) of each
394 station in different watershed against the amplitude of annual signals (Fig. 2b). To quantify the
395 relationship between magnitude of the annual cycle and correlation between the two data sets we fit a
396 linear function between the magnitude of the annual signals and the GPS-GRACE(-FO) [vertical](#)
397 [displacement](#) correlations for each watershed, separately. A steep slope (α) of the fit ($\alpha > 0.5$) indicates an
398 agreement between the two data sets, which depends on the magnitude of the annual cycle. This
399 relationship breaks when stations of a basin exhibit smaller annual cycles. We discuss an interesting case
400 in Supplements, where stations located in the [Great Lakes region \(part of the St. Lawrence watershed\)](#)
401 demonstrate a negative trend $\alpha = -1.26$. The disagreement is even more pronounced while assessing the
402 second metric (i.e., trends). Both metrics, when taken together, helped us identify the source problem (i.e.,
403 unlogged offset [that affected nearly 25% of the stations located in the St. Lawrence watershed](#)) and take
404 corrective actions (see Supplements for more details). Note that for Figs. 2 and 3 the corrected data were
405 used.
406
407

Deleted: deterministic

Deleted: =

Deleted: A +

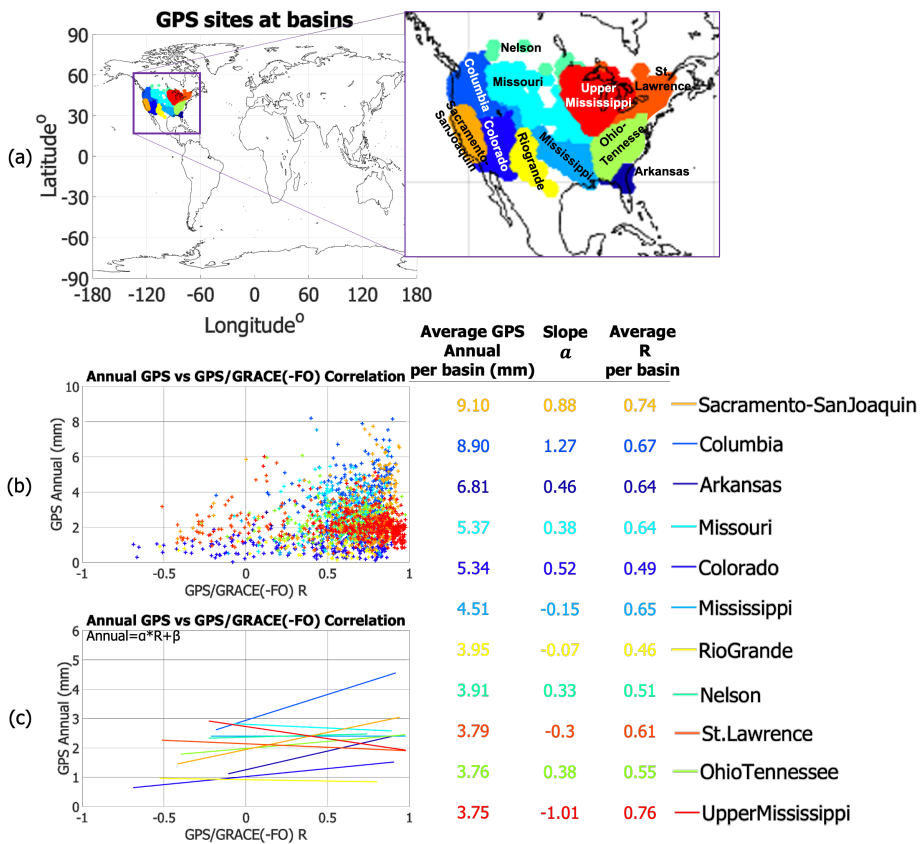
Deleted: amplitude

Deleted: phase

Deleted: with annual frequency

Deleted: VLD

Deleted: basin



416
417
418
419
420
421

Figure 2: a) GPS sites clusters at watersheds in the US. Each watershed has a different color; b) Magnitude of annual GPS vertical displacement cycles derived with respect to GPS-GRACE(-FO) correlation; c) Linear fit between magnitude of the annual GPS vertical displacement cycles and GPS-GRACE(-FO) correlation.

422
423
424

Trends

425
426
427
428
429
430

In order to study the agreement between GPS/GRACE(-FO) in more detail, we split the timeseries of each station into non-overlapping intervals of 36 months, and fit Eq.2 for each station during each time-window. Different time-lengths of the GPS series may lead to misinterpretation of the geophysical content. For example, a station that has records only for the first 13 months out of the total of 36 months window may reflect different fit constituents compared to a neighbor station with full records, if the actual behavior of Earth's response changes during the 36-months window. Although in our data set this

Deleted: VLD
Deleted: VLD

433 case is rare, we proceed with deriving the rate (slope) and the annual cycles only for stations that have
434 records for at least 28 out of the 36 months. [We did not interpolate the series during the GRACE\(-FO\)](#)
435 [gap; thus, the last time-window reflects trends estimated using only GRACE-FO and GPS timeseries](#)
436 [between June 2018-2021](#). As expected, GPS rates feature higher spatial variability than GRACE(-FO).
437 However, both [techniques](#) capture large-scale quasi-periodic variations every 3 years (Fig. 3), an
438 agreement that is noteworthy. The effect of this metric to detect outliers is pronounced when the two
439 [techniques](#) show flipped trends.

Deleted: fairly

Deleted: platforms

Deleted: platforms

440
441 Regions with pronounced trend disagreement:

- 442 • [St. Lawrence watershed \(stations located in the Great Lakes region at the State of Michigan\)](#): The
443 trend during 2015-2018 was flipped between GPS and GRACE(-FO) [in 62 stations \(St. Lawrence](#)
444 [watershed has a total of 243 stations available between 2015-2018\)](#). We discovered a missed
445 offset in the series occurring in April 2016, and corrected for it, which [led to an improved](#)
446 agreement in the trend (see Supplements).
- 447 • Cascadia region (northwest coast): The disagreement is evident in maps spanning 2009-2012,
448 2015-2018 and 2018-2021.5. GPS sites record a large surface uplift, which over the course of 15
449 years sums to 60 mm in sites located in Vancouver Island. GRACE(-FO) does not capture any
450 such behavior. We attribute this disagreement partly on 1) [glacial isostatic adjustment](#) modeling
451 error which manifests oppositely on two [techniques](#). ICE6G D predicts too much subsidence,
452 thus when we correct GPS, we find too much uplift and when we correct GRACE(-FO) we find
453 too much water gain which predicts too much subsidence; and partly on 2) the interseismic strain
454 accumulation correction applied in the GPS data set over this area (Argus et al., 2021). The sites
455 have been flagged and are not going to be used in the joint inversion.
- 456 • San Andreas Fault (Southern California): Sites located in a vicinity of the Parkfield segment of
457 the fault (Carrizon plain), exhibit consistent disagreement in the trend. More investigation is
458 required to understand the mechanism that the fault presents on GPS/GRACE(-FO) [vertical](#)
459 [displacement](#) estimates. The disagreement is also seen in Argus et al. (2022, Fig. S12). The sites
460 have been flagged and are not going to be used in the joint inversion.

Deleted: Great Lakes area (

Deleted:).

Deleted:).

Deleted: the

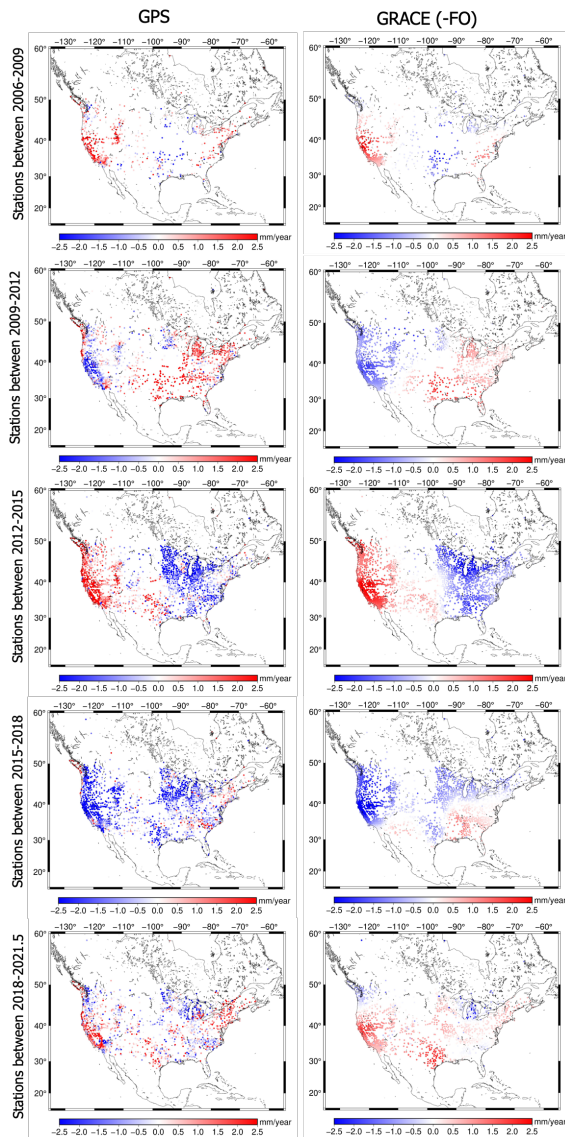
Deleted:).

Deleted: GIA

Deleted: platforms

Deleted:).

Deleted: VLD



474
 475 Figure 3: Rates of vertical displacements derived by GPS and GRACE. The rates are calculated every 36-
 476 months (3 years) between 2006-2021.

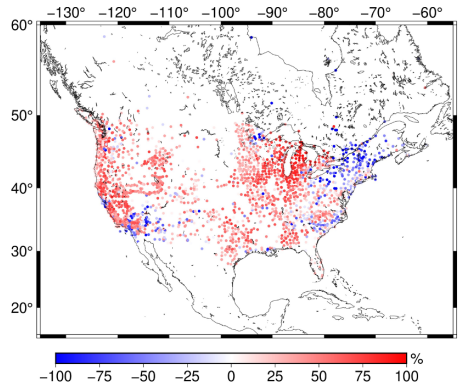
477
 478

479 *Variance Reduction*

480
481 Similarity in both amplitude and phase between two quantities is quantified via the variance attenuation
482 factor (Gaspar and Wunsch, 1989; Fukumori et al., 2015):
483

$$var_{red} = \left(1 - \frac{var(GPS - GRACE(-FO))}{var(GPS)} \right) \times 100 \quad (3)$$

484
485 The higher the agreement in phase and amplitude between GPS and GRACE(-FO), the closer the metric
486 gets to 100%. var_{red} may also be negative when the differences in amplitude and/or phase are large.
487 Overall, GPS and GRACE(-FO) are consistent when var_{red} exceeds 50%. The areas of main
488 disagreement are near coasts, especially along the Atlantic Ocean. This inconsistency can be partly
489 explained by modeling errors of the non-tidal oceanic and atmospheric loading model (e.g., Klos et al.,
490 2021; van Dam et al., 2007). Additionally, agreement is poor for sites located in the vicinity of the
491 Parkfield segment (specific regions across the fault perform poorly), which is consistent with the
492 disagreement shown in Fig. 3.
493



494
495 Figure 4: Variance reduction between GPS and GRACE(-FO) [vertical displacements](#)

496 We also compared the [annual](#) amplitudes of GPS and GRACE(-FO) [vertical displacements \(cosine and](#)
497 [sine components in Eq. 2\)](#). This analysis was not informative for the presence of outliers or errors [in the](#)
498 [current data sample studied](#).

499
500 Overall, the screening process not only assisted in outlier detection, but it also allowed for a deeper look
501 into the structure of [vertical displacement](#) periodic signals. We identified the need for antenna offset
502 corrections (in [sites located in the Great Lakes region](#)); removed sites affected by [glacial isostatic](#)
503 [adjustment](#) and interseismic modeling errors; and sites located at the Parkfield segment of San Andreas
504 Fault.
505
506

Deleted: VLD

Deleted: VLD periodic cycles.

Deleted: .

Deleted: VLD

Deleted: case of

Deleted: GIA

Deleted: ¶

515 **3. Uncertainty Quantification**

516
517 With the updated data set we are now ready to proceed with the uncertainty quantification of the GPS
518 [vertical displacement](#) timeseries. We apply different error characterization schemes consisting of a root
519 sum square of a random error, white noise error, power law noise error (flicker noise and random walk)
520 and spatially coherent error.

Deleted: VLD

521
522 3.1 Methods

523
524 *Root Mean Square Error*

525
526 Residuals r of a series with respect to a [trajectory](#) model (Eq. 2) are often used as a first approximation of
527 noise in [vertical displacement](#) series (e.g., Bos et al., 2013; Michel et al., 2021). Practically, r shows how
528 well a [trajectory](#) model can describe the original time-series. Therefore, the root mean square (rms) of r
529 can give a first approximation of the noise floor of each station.

Deleted: deterministic

Deleted: VLD

Deleted: deterministic

530
531 *Spectral Analysis, White, Flicker and Random Walk Noise*

532
533 Power distribution of residuals and its agreement with noise models, is another popular way to quantify
534 uncertainty of GPS time-series (e.g., Klos et al., 2019; Argus et al., 2022). Typically, GPS series are
535 evaluated for white, flicker and random walk noise, or combination of them. Hector software (Bos et al.,
536 2013) is used to estimate full noise covariance information by means of a maximum likelihood estimator.
537 The covariance matrix C from a combination of white and power law (i.e., flicker and random walk) noise
538 is given as:

Deleted: The

539
|
$$C = a \times \mathbf{I} + b \times \mathbf{J} \tag{Eq. 4}$$

Deleted: I

540
541 Where a is the amplitude of white noise, \mathbf{I} is the identity matrix of size N (number of samples/epochs in
542 the series), b is the amplitude and \mathbf{J} the covariance matrix of power law noise. \mathbf{J} matrix is a full
543 covariance matrix that describes the time-correlated error (as the data record length increases, the
544 displacement uncertainty changes (Bos et al., 2008 Eqs. 8-11)). The optimal selection of the noise models
545 is done via two optimality criteria, namely the Akaike Information Criterion (Akaike, 1974) and the
546 Bayesian Criterion (Schwarz, 1978).

547
548 In this study, we consider three cases:

- 549 a) White Noise (WN)
- 550 b) Combination of WN and Flicker Noise (WN+FN)
- 551 c) Combination of WN, FN and Random Walk Noise (WN+FN+RW)

552 We take the root-sum-squares of the noise magnitudes as our noise floor. For example, for the case of
553 WN+FN noise, noise is derived as $\sigma = \pm \sqrt{\sigma_{WN}^2 + \sigma_{FN}^2}$. Our data are sampled on a monthly basis, thus

560 σ_{FN} needs to be scaled appropriately, i.e., $\sigma_{FN} = \sigma_{PL} \left(\frac{1}{12}\right)^{\frac{k}{4}}$, where, σ_{PL} is the uncertainty of power-law
 561 (PL) and k the spectral index, outputted from Hector (more information on power-law noise estimation
 562 can be found in Bos et al., 2008, and Williams, 2003).

563
 564 *Common Mode Noise*

565
 566 The Common Mode Component (CMC) is derived following the processing scheme suggested by
 567 Kreemer and Blewitt (2021), which can be summarized as:

- 568
 569 1) Input GPS [displacement](#) time-series (referenced to Sep 2012) for j stations (l_j)
 570 2) Derive each station's residuals by removing the [trajectory](#) part of the series ($l_j(t) - y_j(t)$)
 571 3) Quantify the correlation coefficient r_{MAD} using robust statistics. r_{MAD} is defined as:

$$r_{MAD} = \frac{MAD^2(u) - MAD^2(v)}{MAD^2(u) + MAD^2(v)} \quad \text{Eq. 5}$$

572
 573 [The median absolute deviation \(MAD\) is the absolute deviation around the median. For example, for a](#)
 574 [residual series res\(t\) \$MAD = |res\(t\) - median\(res\(t\)\)\$.](#) u and v are derived as:

$$u = \frac{p - median(p)}{\sqrt{2}MAD(p)} + \frac{q - median(q)}{\sqrt{2}MAD(q)} \quad \text{Eq. 6}$$

$$v = \frac{p - median(p)}{\sqrt{2}MAD(p)} - \frac{q - median(q)}{\sqrt{2}MAD(q)} \quad \text{Eq. 7}$$

575
 576 with p and q being the residual series of the reference station and the neighbor station, respectively.
 577 For each station there are $j - 1$ correlation coefficients r_{MAD} . In order to decide the cut-off distance
 578 that a neighbor station will be considered in the analysis we plot r_{MAD} coefficient against its distance
 579 from the reference station (Fig. 5). Based on results from all stations we decide to set a cut-off at 1500
 580 km, slightly higher than the 1350 km suggested by Kreemer and Blewitt (2021). The 1500 km cut-off
 581 allows us to separate stations between [East](#) and [West](#) coast, as spatially coherent signals at stations
 582 located across the continent are negligible.

- 583 4) Derive the median slope estimator (ccs) using Theil-Sen median trend. [ccs is the median trend of the](#)
 584 [r_{MAD} coefficients of a station against their distance with the reference station.](#)
 585 5) Derive the zero-distance intercept cci_j for each station as $median(r_{MAD} - ccs * d)$, with d being the
 586 distance between the station of reference and the neighbor station (maximum $d = 1500$ km).

Deleted: VLD

Deleted: deterministic

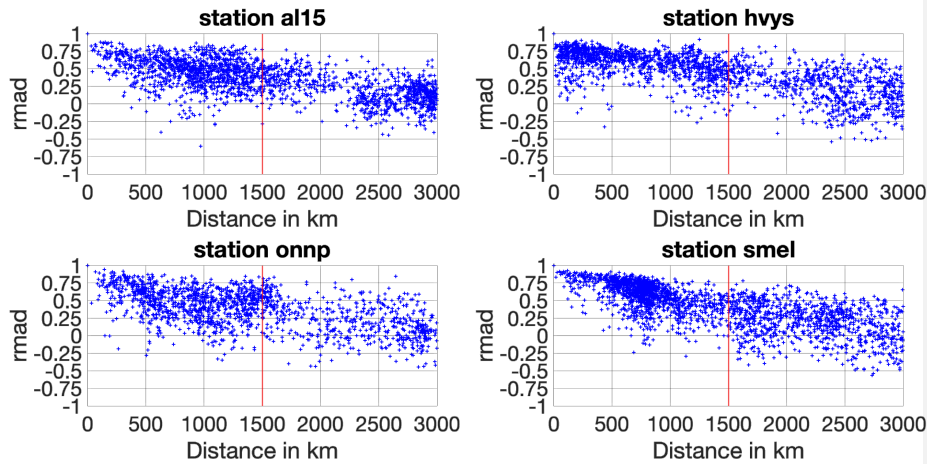
Deleted: where MAD is the

Deleted: value and

Deleted: east

Deleted: west

593 6) Construct CMC: Calculate the cumulative (c_j) and percentile (p_j) weights for each station and then
 594 find the weighted median that corresponds to $p_j = 50\%$. This weighted median represents the CMC of
 595 the station (Fig. 6).



596 Figure 5: r_{MAD} coefficient of four random stations with the rest of the station sample, plotted against the
 597 distance of the reference station with the rest of the stations. Each cross resembles the of the reference
 598 station with a station located at distance d .

601 CMC is limited in providing a realistic error approximation, in that the technique cannot isolate spatially
 602 correlated noise from signal (e.g., hydrology signals not described by the [trajectory](#) model are present in
 603 the residuals fed into CMC). Under the realistic assumption that a component of the high frequency signal
 604 contained in CMC reflects real hydrological processes, we remove the contribution of surface hydrology
 605 using Global Land Data Assimilation System (GLDAS) (Rodell et al., 2004) [vertical displacement](#)
 606 [estimates](#). GLDAS does not model deep groundwater and open surface water, so these signals remain in
 607 the residual (Scanlon et al., 2018). [Vertical displacement estimates](#) driven by surface hydrology are
 608 derived similar to GRACE(-FO) (Section 2.2). We use Noah v2.1 monthly estimates of soil moisture
 609 storage given at 0.25-degree grids (Beaudoing and Rodell, 2016), convert the fields from terrestrial water
 610 storage (kg/m^2) to units of equivalent water height, [derive the spherical harmonic coefficients of the](#)
 611 [equivalent water height mass load using Wahr et al. \(1998\)](#), and predict the elastic response of the Earth
 612 (Eq. 1). [Afterwards, we remove the reference epoch \(09/2012\) similar to GPS and estimate the up](#)
 613 [displacement at the locations of the GPS sites by interpolating the estimates of the closest neighbors to the](#)
 614 [station's location. Note, that because our interest is to prepare the data for a combined solution with](#)
 615 [GRACE\(-FO\) we interpolate the timeseries at the times of GRACE\(-FO\) monthly series availability. The](#)
 616 [interested reader is referred to the supplement, where we show the up displacement estimated by GPS,](#)
 617 [GRACE\(-FO\) and GLDAS \(Figure S2\) for randomly selected stations. Finally, we derive residuals](#)
 618 relative to the [trajectory](#) model (Eq. 2). GLDAS (surface hydrology) residuals should ideally reflect high
 619 frequency hydrological processes and are therefore removed from GPS residuals. Overall, CMC of
 620 surface hydrology residuals exhibits a fairly small magnitude (~ 0.5 mm). We remove the contribution of
 621 surface hydrology within the CMC algorithm by first subtracting GLDAS [vertical displacement estimates](#)

Deleted: deterministic

Deleted: VLD predictions

Deleted: VLD predictions

Deleted: Finally

Deleted: VLDs and derive the

Deleted: deterministic

Deleted: VLD predictions

629 from GPS, and next inputting the residuals of this difference into the algorithm. The output of this process
 630 (CMC_{HF}) slightly decreases the magnitude of CMC and expresses a more realistic representation of
 631 spatially correlated noise.

632
 633 3.2 Results

634
 635 Vertical displacement uncertainty of each station is estimated by means of all the different approaches
 636 discussed in Section 3. Mean (μ), median and standard deviation (std) values are shown in Table 1. On
 637 average, an assumption of white noise shows slightly reduced uncertainty compared to the other
 638 techniques, followed by RMSE. When flicker noise is considered in addition to white noise (WN+FN) the
 639 average uncertainty increases by nearly 0.8 mm compared to the white noise only. We note that the
 640 contribution of white noise in the case of WN+FN is negligible for ninety seven percent of the stations
 641 (that is flicker noise describes the noise exclusively). Noise level from combination of all three noise
 642 models (WN+FN+RW) is less than 4 mm on average. In this case too, white noise is negligible, and noise
 643 is described exclusively from flicker noise for 1550 stations, and from random walk for 600 stations. The
 644 rest of the data sample reflects a contribution from both noise models. We additionally analyzed the
 645 amplitude of the noise of each noise model (σ_{PI}) with respect to the length of the input series. Results did
 646 not identify any clear relationship between σ_{PI} and the length of each station's timeseries. CMC noise
 647 floor is 3.6 mm on average with a relatively large standard deviation (± 1.6 mm) which suggests that
 648 spatially correlated noise has higher variability than time-correlated noise (± 1.6 mm as opposed to $\sim \pm 1$
 649 mm). When surface hydrology is removed (CMC_{HF}) the noise floor drops by a fraction of a mm on
 650 average compared to CMC.

651
 652 Table 1: Different uncertainty quantification cases

	<u>mean (μ)</u> (mm)	median (mm)	\pm std (mm)
RMSE	2.8	2.7	0.8
WN	2.4	2.2	0.8
WN+FN	3.2	3.1	0.7
WN+FN+RW	3.8	3.5	1.1
CMC	3.6	3.2	1.6
CMC _{HF}	3.5	3.1	1.6

653
 654 RMSE and WN exhibit a smooth transition among the regions, which indicates the presence of spatially
 655 coherent regime signal mostly driven by hydrology (Fig. 6). The combination of WN+FN is mostly
 656 dominated by FN and the uncertainty exhibits local (in space) coherence. The uncertainty is larger when
 657 random walk is included in the combination (WN+FN+RW). A recent study from Argus et al. (2022) on
 658 groundwater flux in Central Valley (California) suggests that noise on GPS-derived uplift motion can be
 659 well described by a combination of flicker noise and random walk, due to the ability of these noise
 660 models to reflect low frequency noise. When a simulated contribution of the surface hydrological
 661 component is removed from the series, CMC_{HF} reflects a more realistic picture of the noise. Arguably the

Deleted: VLD

Deleted: The mean value

Deleted: Noise level from combination of all three noise models (WN+FN+RW) is somewhat less than 4 mm on average....

667 level of change compared to CMC is sub-millimeter. Signal contributions from un-modelled groundwater
668 variations are potentially still present, but groundwater changes are typically slower in time.

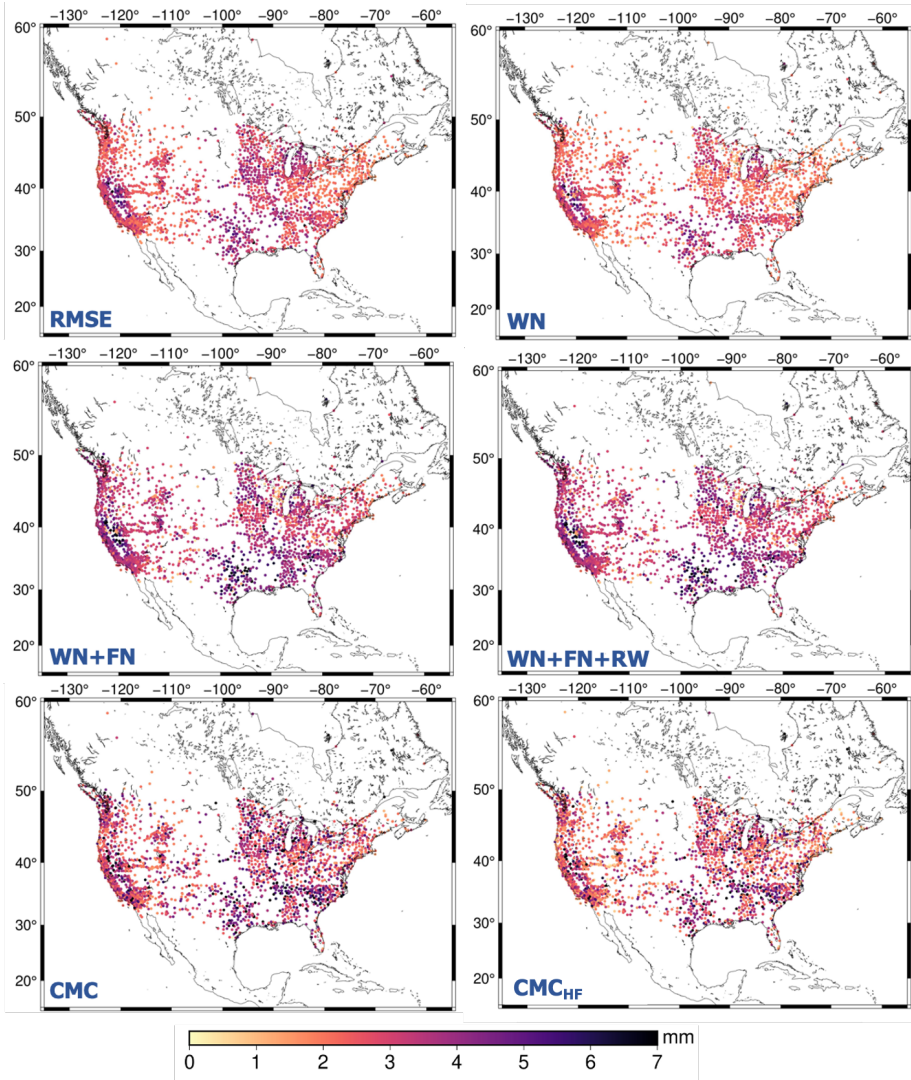
669

670

671 We obtain the relative likelihood of each uncertainty quantification method by estimating the probability
672 density function (PDF) (Fig. 7). White noise has a flat power spectrum, having the same amplitude
673 across frequencies. Estimating a best fit for a flat spectrum doesn't allow for capturing the long tail skew
674 of the residuals (low frequency), which are biased towards their mean. Thus, the amplitude of white noise
675 is smaller compared to the rest of the techniques (Table 1). Flicker and random walk noise models add to
676 the long tail of the power distribution, that is they allow more low frequency noise, which explains the
677 higher amplitude of the uncertainty when these two noise types are considered.

678 RMSE and WN show a 50% probability of a station having an uncertainty (σ) between 1.5-2 mm and less
679 than 10% of a station exceeding $\sigma=4$ mm. The noise level falls within [2 4] mm for ~93% of the stations
680 when we consider combination of WN+FN. PDF of RMSE, WN and WN+FN resemble a normal
681 distribution, with the mean being shifted for each case. When random walk is also considered
682 (WN+FN+RW) 64% of the stations exhibit noise within [2 4] mm. In this case, the distribution is more
683 spread resembling a gamma-like distribution, with a peak being at 3 mm (18%). CMC and CMC_{HF} PDF
684 also follow a gamma-shape, and the probability of the uncertainty ranging between [2 4] mm is nearly
685 60% for CMC and 65% when surface hydrology is removed.

686



687
688
689

Figure 6: Uncertainty of GPS [timeseries](#) estimated using various techniques.

Deleted: sites

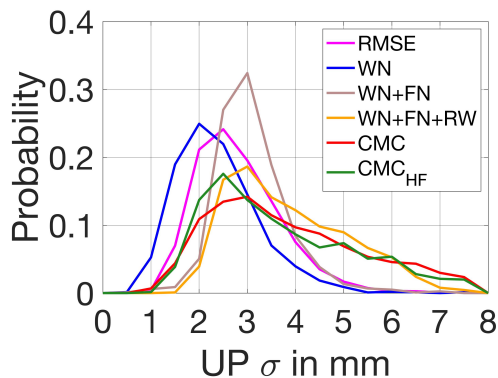


Figure 7: Probability density function of vertical displacement estimates uncertainty

4. Discussion

GPS-derived vertical displacements are very useful for supplementing GRACE(-FO) gravity products to infer mass change signals at spatial scales smaller than what can typically be achieved with current satellite gravimetry alone (i.e., < 300km). This work provides a general workflow to isolate elastic surface mass signals from GPS vertical displacement, by developing processing standards; additionally, it suggests uncertainty quantification schemes to quantify error on GPS vertical displacement estimates. The ultimate goal is to prepare GPS estimates for merging with satellite-gravimetry observations. First, we provide a list of corrections needed for isolating surface mass following recommendations outlined in Argus et al. (2017; 2022). Additionally, a detailed investigation of trends, correlation, and variance reduction highlights the need for better background modeling (glacial isostatic adjustment and interseismic strain), as the two observation techniques respond differently in the presence of such errors. At this point the recommendation is to remove sites located in the vicinity of regions where background models are known to perform poorly, before any joint inversion. Except detecting outlier stations, screening metrics point to extra corrections that need to be applied in certain sites (e.g., missed antenna offsets).

Several uncertainty quantification schemes have been tested to prescribe weights on GPS vertical displacement estimates that are needed for a joint inversion with GRACE(-FO) data. The average noise level indicated by RMSE is 2.8 mm. White noise average is 2.5 mm. The errors increase when lower frequencies are included in the noise estimation. When we account for flicker noise, one third of the sites exhibits noise levels of up to 3 mm. The average noise increases significantly in presence of random walk, as more power of the lower frequencies gets into the estimations, and the distribution of noise is more dispersed. In this case, half of the stations are prescribed with > 4 mm uncertainty. Argus et al. (2022), finds that random walk is the most realistic representation of noise based on postfit residuals. We notice that the spectrum of CMC provides similar uncertainties to random walk, which implies that despite the different characterization procedure, CMC is able to provide equally realistic noise estimates of GPS timeseries. We attempted to minimize lingering hydrology signals embedded in CMC, through

Deleted: VLD

Deleted: VLD observations

Deleted: to supplement

Deleted: on isolating

Deleted: ,

Deleted: and

Deleted: of GPS VLD

Deleted: , with the

Deleted: of

Deleted: them

Deleted: , accentuates

Deleted: GIA

Deleted: platforms

Deleted: offset in sites located in Michigan

Deleted: VLD

Deleted: the

Deleted: .

Deleted: is centered at 2 and 2.5 mm when uncertainty is derived as the

Deleted: of residuals or as white

Deleted: , respectively. Error increases

Deleted: suggests

Deleted: VLD

Deleted: strived

745 reducing the GPS [vertical displacement](#) observations with [displacements](#) from the GLDAS hydrology
746 model. The average noise floor dropped slightly (~0.5 mm drop in sigma). Future work will provide
747 further information of GPS station errors when the weight of each GPS site is also considered based on its
748 impact on the performance in a formal data combination of GPS-GRACE(-FO). The suggested
749 framework can be easily adjusted to account for global data sets. The new data set provides GPS vertical
750 displacements of elastic mass variations in North America and their [associated](#) uncertainties.

Deleted: VLD

Deleted: VLD

Deleted: potentially

751
752 **Data Availability:** The data product described in the manuscript is available in zenodo (doi:
753 <https://zenodo.org/record/8184285>). GPS timeseries are provided by the Global Station List from the
754 Nevada Geodetic Laboratory (<http://geodesy.unr.edu/>; Blewitt et al., 2018). Non atmospheric and oceanic
755 tidal aliasing product (AOD1B RL06) is provided by GFZ's Information System and Data Center
756 (<ftp://isdg.gfz-potsdam.de/grace/Level-1B/GFZ/AOD/RL06>, Dobslaw et al., 2017). GRACE and
757 GRACE-FO Level 2 products are available from odaac (<https://doi.org/10.5067/GFL20-MJ060>).

Deleted: 10.5281/zenodo.8184285).

758
759 **Acknowledgments:** The research was carried out at the Jet Propulsion Laboratory, California Institute
760 of Technology, under a contract with the National Aeronautics and Space Administration
761 (80NM0018D0004). Maps were made with the Generic Mapping Toolbox (Wessel et al. 2019).

762 **References**

- 763
764
765 Akaike, H.: A new look at the statistical model identification. IEEE transactions on automatic control,
766 19(6), pp.716-723. <https://doi.org/10.1109/TAC.1974.1100705>, 1974.
- 767
768 Altamimi, Z., Rebischung, P., Métivier, L. and Collilieux, X.: ITRF2014: A new release of the
769 International Terrestrial Reference Frame modeling nonlinear station motions. Journal of Geophysical
770 Research: Solid Earth, 121(8), pp.6109-6131. <https://doi.org/10.1002/2016JB013098>, 2016.
- 771
772 Amiri-Simkooei, A.R., Mohammadloo, T.H. and Argus, D.F.: Multivariate analysis of GPS position time
773 series of JPL second reprocessing campaign. Journal of Geodesy, 91, pp.685-704.
774 <https://doi.org/10.1007/s00190-016-0991-9>, 2017.
- 775
776 Argus, D.F., Fu, Y. and Landerer, F.W.: Seasonal variation in total water storage in California inferred
777 from GPS observations of vertical land motion. Geophysical Research Letters, 41(6), pp.1971-1980.
778 <https://doi.org/10.1002/2014GL059570>, 2014.
- 779
780 Argus, D.F., Gordon, R.G., Heflin, M.B., Ma, C., Eanes, R.J., Willis, P., Peltier, W.R. and Owen, S.E.:
781 The angular velocities of the plates and the velocity of Earth's centre from space geodesy. Geophysical
782 Journal International, 180(3), pp.913-960. <https://doi.org/10.1111/j.1365-246X.2009.04463.x>, 2010.
- 783
784 Argus, D.F., Landerer, F.W., Wiese, D.N., Martens, H.R., Fu, Y., Famiglietti, J.S., Thomas, B.F., Farr,
785 T.G., Moore, A.W. and Watkins, M.M.: Sustained water loss in California's mountain ranges during
786 severe drought from 2012 to 2015 inferred from GPS. Journal of Geophysical Research: Solid Earth,
787 122(12), pp.10-559. <https://doi.org/10.1002/2017JB014424>, 2017.

Deleted:

794 [Argus, D. F., Peltier, W. R., Drummond, R. and Moore, A. W: The Antarctica component of postglacial](#)
795 [rebound model ICE-6G C \(VM5a\) based on GPS positioning, exposure age dating of ice thicknesses, and](#)
796 [relative sea level histories. Geophysical Journal International, 198, 537–563.](#)
797 <https://doi.org/10.1093/gji/ggu140>, 2014.

798
799 Argus, D.F., Martens, H.R., Borsa, A.A., Knappe, E., Wiese, D.N., Alam, S., Anderson, M., Khatiwada,
800 A., Lau, N., Peidou, A. and Swarr, M.: Subsurface water flux in California's Central Valley and its source
801 watershed from space geodesy. *Geophysical Research Letters*, 49(22), p.e2022GL099583.
802 <https://doi.org/10.1029/2022GL099583>, 2022.

803
804 Argus, D.F., Peltier, W.R., Blewitt, G. and Kreemer, C.: The Viscosity of the Top Third of the Lower
805 Mantle Estimated Using GPS, GRACE, and Relative Sea Level Measurements of Glacial Isostatic
806 Adjustment. *Journal of Geophysical Research: Solid Earth*, 126(5), p.e2020JB021537.
807 <https://doi.org/10.1029/2020JB021537>, 2021.

808
809 Beaudoin, H. and M. Rodell: GLDAS Noah Land Surface Model L4 monthly 0.25 x 0.25 degree V2.1,
810 Greenbelt, Maryland, USA, Goddard Earth Sciences Data and Information Services Center (GES DISC).
811 <https://doi.org/10.5067/SXAVCZFAQLNO>, 2020.

812
813 Becker, J.M. and Bevis, M.: Love's problem. *Geophysical Journal International*, 156(2), pp.171-178.
814 <https://doi.org/10.1111/j.1365-246X.2003.02150.x>, 2004.

815
816 Bertiger, W., Bar-Sever, Y., Dorsey, A., Haines, B., Harvey, N., Hemberger, D., Heflin, M., Lu, W.,
817 Miller, M., Moore, A.W. and Murphy, D.: GipsyX/RTGx, a new tool set for space geodetic operations
818 and research. *Advances in space research*, 66(3), pp.469-489. <https://doi.org/10.1016/j.asr.2020.04.015>,
819 2020.

820
821 [Bevis, M. and Brown, A.: Trajectory models and reference frames for crustal motion geodesy \(2014\).](#)
822 [Journal of Geodesy, 88, 283–311, doi: 10.1007/s00190-013-0685-5.](#)

823
824 Blewitt, G., Hammond, W.C. and Kreemer, C.: Harnessing the GPS data explosion for interdisciplinary
825 science. *Eos*, 99(10.1029), p.485. doi.org/10.1029/2018EO104623.
826 <https://doi.org/10.1029/2018EO104623>, 2018.

827
828 Blewitt, G., Lavallée, D., Clarke, P. and Nurutdinov, K.: A new global mode of Earth deformation:
829 Seasonal cycle detected. *Science*, 294(5550), pp.2342-2345.
830 <https://doi.org/10.1126/science.1065328>, 2001.

831
832 [Boehm, J., Werl, B., and Schuh, H.: Troposphere mapping functions for GPS and very long baseline](#)
833 [interferometry from European Centre for Medium-Range Weather Forecasts operational analysis data, *J.*](#)
834 [Geophys. Res.](#), 111, B02406, doi:10.1029/2005JB003629, 2006.

835

Deleted: .., 2018.

837 Borsa, A.A., Agnew, D.C. and Cayan, D.R.: December. Drought-induced uplift in the western United
838 States as observed by the EarthScope Plate Boundary Observatory GPS network. In AGU Fall Meeting
839 Abstracts (Vol. 2014, pp. G23B-0481), 2014.

840

841 Bos, M.S., Fernandes, R.M.S., Williams, S.D.P. and Bastos, L.: Fast error analysis of continuous GPS
842 observations. *Journal of Geodesy*, 82(3), pp.157-166. <https://doi.org/10.1007/s00190-007-0165-x>, 2008.

843

844 Bos, M.S., Fernandes, R.M.S., Williams, S.D.P. and Bastos, L.: Fast error analysis of continuous GPS
845 observations with missing data. *Journal of Geodesy*, 87(4), pp.351-360. <https://doi.org/10.1007/s00190-012-0605-0>, 2013.

846

847

848 Chew, C.C. and Small, E.E.: Terrestrial water storage response to the 2012 drought estimated from GPS
849 vertical position anomalies. *Geophysical Research Letters*, 41(17), pp.6145-6151.
850 <https://doi.org/10.1002/2014GL061206>, 2014.

851

852 Crowell, B.W., Bock, Y. and Liu, Z.: Single-station automated detection of transient deformation in GPS
853 time series with the relative strength index: A case study of Cascadian slow slip. *Journal of Geophysical
854 Research: Solid Earth*, 121(12), pp.9077-9094. <https://doi.org/10.1002/2016JB013542>, 2016.

855

856 Davis, J.L., Elósegui, P., Mitrovica, J.X. and Tamisiea, M.E.: Climate-driven deformation of the solid
857 Earth from GRACE and GPS. *Geophysical Research Letters*, 31(24).
858 <https://doi.org/10.1029/2004GL021435>, 2004.

859

860 Dee, D.P., Uppala, S.M., Simmons, A.J., Berrisford, P., Poli, P., Kobayashi, S., Andrae, U., Balmaseda,
861 M.A., Balsamo, G., Bauer, D.P. and Bechtold, P.: The ERA-Interim reanalysis: Configuration and
862 performance of the data assimilation system. *Quarterly Journal of the royal meteorological society*,
863 137(656), pp.553-597. <https://doi.org/10.1002/qj.828>, 2011.

864

865 [Dill, R., and Dobslaw, H.: Numerical simulations of global-scale high resolution hydrological crustal
866 deformations. *Journal of Geophysical Research: Solid Earth*, 118\(9\), 5008–5017.
867 <https://doi.org/10.1002/jgrb.50353>, 2013.](https://doi.org/10.1002/jgrb.50353)

868

869 Dobslaw, H., Bergmann-Wolf, I., Dill, R., Poropat, L., Thomas, M., Dahle, C., Esselborn, S., König, R.
870 and Flechtner, F.: A new high-resolution model of non-tidal atmosphere and ocean mass variability for
871 de-aliasing of satellite gravity observations: AOD1B RL06. *Geophysical Journal International*, 211(1),
872 pp.263-269. <https://doi.org/10.1093/gji/ggx302>, 2017.

873

874 [Dong, D., Fang, P., Bock, Y., Webb, F., Prawirodirdjo, L., Kedar, S., and Jamason, P.: Spatiotemporal
875 filtering using principal component analysis and Karhunen-Loeve expansion approaches for regional GPS
876 network analysis. *J. Geophys. Res.*, 111, B03405, <https://doi.org/10.1029/2005JB003806>, 2006.](https://doi.org/10.1029/2005JB003806)

877

878 Frederikse, T., Landerer, F., Caron, L., Adhikari, S., Parkes, D., Humphrey, V.W., Dangendorf, S.,
879 Hogarth, P., Zanna, L., Cheng, L. and Wu, Y.H.: The causes of sea-level rise since 1900. *Nature*,
880 584(7821), pp.393-397. <https://doi.org/10.1038/s41586-020-2591-3>, 2020.

881
882 Fu, Y. and Freymueller, J.T.: Seasonal and long-term vertical deformation in the Nepal Himalaya
883 constrained by GPS and GRACE measurements. *Journal of Geophysical Research: Solid Earth*, 117(B3).
884 <https://doi.org/10.1029/2011JB008925>, 2012.
885
886 Fu, Y., Argus, D.F. and Landerer, F.W.: GPS as an independent measurement to estimate terrestrial water
887 storage variations in Washington and Oregon. *Journal of Geophysical Research: Solid Earth*, 120(1),
888 pp.552-566. <https://doi.org/10.1002/2014JB011415>, 2015.
889
890 Fukumori, I., Wang, O., Llovel, W., Fenty, I. and Forget, G.: A near-uniform fluctuation of ocean bottom
891 pressure and sea level across the deep ocean basins of the Arctic Ocean and the Nordic Seas. *Progress in*
892 *Oceanography*, 134, pp.152-172. <https://doi.org/10.1016/j.pocean.2015.01.013>, 2015.
893
894 Gazeaux, J., Williams, S., King, M., Bos, M., Dach, R., Deo, M., Moore, A.W., Ostini, L., Petrie, E.,
895 Roggero, M. and Teferle, F.N.: Detecting offsets in GPS time series: First results from the detection of
896 offsets in GPS experiment. *Journal of Geophysical Research: Solid Earth*, 118(5), pp.2397-2407.
897 <https://doi.org/10.1002/jgrb.50152>, 2013.
898
899 [Haines, B., Bar-Sever, Y., Bertiger, W., Desai, S. and Willis, P. One-centimeter orbit determination for](https://doi.org/10.1007/BF03321179)
900 [Jason-1: new GPS-based strategies. *Marine Geodesy*, 27\(1-2\), pp.299-318.](https://doi.org/10.1007/BF03321179)
901 <https://doi.org/10.1007/BF03321179>, 2004.
902
903 [Hammond, W. C., Blewitt, G., and Kreemer, C.: GPS Imaging of vertical land motion in California and](https://doi.org/10.1002/2016JB013458)
904 [Nevada: Implications for Sierra Nevada uplift, *J. Geophys. Res. Solid Earth*, 121, 7681–7703,](https://doi.org/10.1002/2016JB013458)
905 [doi:10.1002/2016JB013458](https://doi.org/10.1002/2016JB013458), 2016.
906
907 He, X., Bos, M.S., Montillet, J.P. and Fernandes, R.M.S.: Investigation of the noise properties at low
908 frequencies in long GPS time series. *Journal of Geodesy*, 93(9), pp.1271-1282.
909 <https://doi.org/10.1007/s00190-019-01244-y>, 2019.
910
911 Houborg, R., Rodell, M., Li, B., Reichle, R. and Zaitchik, B.F.: Drought indicators based on model-
912 assimilated Gravity Recovery and Climate Experiment (GRACE) terrestrial water storage observations.
913 *Water Resources Research*, 48(7). <https://doi.org/10.1029/2011WR011291>, 2012.
914
915 Ji, K.H. and Herring, T.A. A method for detecting transient signals in GPS position time-series:
916 smoothing and principal component analysis. *Geophysical Journal International*, 193(1), pp.171-186.
917 <https://doi.org/10.1093/gji/ggt003>, 2013.
918
919 Jiang, W., Li, Z., van Dam, T. and Ding, W.: Comparative analysis of different environmental loading
920 methods and their impacts on the GPS height time series. *Journal of Geodesy*, 87(7), pp.687-703.
921 <https://doi.org/10.1007/s00190-013-0642-3>, 2013.
922

923 Klos, A., Bogusz, J., Figurski, M. and Kosek, W.: Uncertainties of geodetic velocities from permanent
924 GPS observations: the Sudeten case study. *Acta Geodynamica et Geomaterialia*, 11(3), p.175.
925 <https://doi.org/10.13168/AGG.2014.0005>, 2014.
926
927 Klos, A., Dobsław, H., Dill, R. and Bogusz, J.: Identifying the sensitivity of GPS to non-tidal loadings at
928 various time resolutions: examining vertical displacements from continental Eurasia. *GPS Solutions*,
929 25(3), p.89. <https://doi.org/10.1007/s10291-021-01135-w>, 2021.
930
931 Klos, A., Kusche, J., Fenoglio-Marc, L., Bos, M.S. and Bogusz, J.: Introducing a vertical land
932 displacement model for improving estimates of sea level rates derived from tide gauge records affected by
933 earthquakes. *GPS Solutions*, 23(4), pp.1-12. <https://doi.org/10.1007/s10291-019-0896-1>, 2019.
934
935 Kreemer, C. and Blewitt, G.: Robust estimation of spatially varying common-mode components in GPS
936 time-series. *Journal of geodesy*, 95(1), pp.1-19. <https://doi.org/10.1007/s00190-020-01466-5>, 2021.
937
938 Kumar, U., Chao, B.F. and Chang, E.T.: What causes the common-mode error in array GPS displacement
939 fields: Case study for Taiwan in relation to atmospheric mass loading. *Earth and Space Science*, 7(11),
940 p.e2020EA001159. <https://doi.org/10.1029/2020EA001159>, 2020.
941
942 Landerer, F.W., Flechtner, F.M., Save, H., Webb, F.H., Bandikova, T., Bertiger, W.I., Bettadpur, S.V.,
943 Byun, S.H., Dahle, C., Dobsław, H. and Fahnestock, E.: Extending the global mass change data record:
944 GRACE Follow-On instrument and science data performance. *Geophysical Research Letters*, 47(12),
945 p.e2020GL088306. <https://doi.org/10.1029/2020GL088306>, 2020.
946
947 Li, S., Wang, K., Wang, Y., Jiang, Y. and Dosso, S.E.: Geodetically inferred locking state of the Cascadia
948 megathrust based on a viscoelastic Earth model. *Journal of Geophysical Research: Solid Earth*, 123(9),
949 pp.8056-8072. <https://doi.org/10.1029/2018JB015620>, 2018.
950
951 Li, W. and Shen, Y.: The consideration of formal errors in spatiotemporal filtering using principal
952 component analysis for regional GPS position time series. *Remote Sensing*, 10(4), p.534.
953 <https://doi.org/10.3390/rs10040534>, 2018.
954
955 Liu, B., Dai, W., Peng, W. and Meng, X.: Spatiotemporal analysis of GPS time series in vertical direction
956 using independent component analysis. *Earth, Planets and Space*, 67(1), pp.1-10.
957 <https://doi.org/10.1186/s40623-015-0357-1>, 2015.
958
959 Loomis, B.D., Rachlin, K.E. and Luthcke, S.B.: Improved Earth oblateness rate reveals increased ice
960 sheet losses and mass-driven sea level rise. *Geophysical Research Letters*, 46(12), pp.6910-6917.
961 <https://doi.org/10.1029/2019GL082929>, 2019.
962
963 [Martens, H. R., Argus, D. F., Norberg, C., Blewitt, G., Herring, T. A., Moore, A. W., et al.: Atmospheric](https://doi.org/10.1007/s00190-020-01445-w)
964 [pressure loading in GPS positions: Dependency on GPS processing methods and effect on assessment of](https://doi.org/10.1007/s00190-020-01445-w)
965 [seasonal deformation in the contiguous USA and Alaska. *Journal of*](https://doi.org/10.1007/s00190-020-01445-w)
966 [Geodynamics](https://doi.org/10.1007/s00190-020-01445-w), 94(12), 115. <https://doi.org/10.1007/s00190-020-01445-w>, 2020.

967
968 Michel, A., Santamaría-Gómez, A., Boy, J.P., Perosanz, F. and Loyer, S.: Analysis of GPS Displacements
969 in Europe and Their Comparison with Hydrological Loading Models. *Remote Sensing*, 13(22), p.4523.
970 <https://doi.org/10.3390/rs13224523>, 2021.
971
972 Milliner, C., Materna, K., Bürgmann, R., Fu, Y., Moore, A.W., Bekaert, D., Adhikari, S. and Argus, D.F.:
973 Tracking the weight of Hurricane Harvey's stormwater using GPS data. *Science advances*, 4(9),
974 p.eaau2477. <https://doi.org/10.1126/sciadv.aau2477>, 2018.
975
976 Montillet, J.P., Melbourne, T.I. and Szeliga, W.M.: GPS vertical land displacement corrections to sea-
977 level rise estimates in the Pacific Northwest. *Journal of Geophysical Research: Oceans*, 123(2), pp.1196-
978 1212. <https://doi.org/10.1002/2017JC013257>, 2018.
979
980 Nikolaidis, R.: Observation of geodetic and seismic deformation with the Global Positioning System.
981 University of California, San Diego, 2002.
982
983 Pail, R., Bingham, R., Braitenberg, C., Dobslaw, H., Eicker, A., Güntner, A., Horwath, M., Ivins, E.,
984 Longuevergne, L., Panet, I. and Wouters, B.: Science and user needs for observing global mass transport
985 to understand global change and to benefit society. *Surveys in Geophysics*, 36(6), pp.743-772.
986 <https://doi.org/10.1007/s10712-015-9348-9>, 2015.
987
988 [Peltier, W. R., Argus, D. F. and Drummond, R.: Space geodesy constrains ice age terminal deglaciation:
989 The global ICE-6G_C \(VM5a\) model. *Journal Geophysical Research: Solid Earth*, 120, 450–487.
990 <https://doi.org/10.1002/2014JB011176>, 2015.](https://doi.org/10.1002/2014JB011176)
991
992 Peltier, W. R., Argus, D. F., and Drummond, R.: Comment on the paper by Purcell et al. 2016 entitled 'An
993 assessment of ICE-6G_C (VM5a) glacial isostatic adjustment model (2018). *Journal Geophysical*
994 *Research: Solid Earth*, 122, 2019-2028. <https://doi.org/10.1002/2016JB013844>, 2018.
995
996 [Luzum, B. and Petit, G. \(2012\). The IERS Conventions: Reference systems and new models. *Proceedings*
997 *of the International Astronomical Union*, 10\(H16\), 227-228. \[https://doi:10.1017/S1743921314005535\]\(https://doi.org/10.1017/S1743921314005535\),
998 \[2012.\]\(https://doi.org/10.1017/S1743921314005535\)
999
1000 Ray, J., Altamimi, Z., Collilieux, X. and van Dam, T.: Anomalous harmonics in the spectra of GPS
1001 position estimates. *GPS solutions*, 12, pp.55-64. <https://doi.org/10.1007/s10291-007-0067-7>, 2008.
1002
1003 Reager, J.T., Thomas, B.F. and Famiglietti, J.S.: River basin flood potential inferred using GRACE
1004 gravity observations at several months lead time. *Nature Geoscience*, 7\(8\), pp.588-592.
1005 <https://doi.org/10.1038/ngeo2203>, 2014.
1006
1007 Rodell, M., Houser, P.R., Jambor, U.E.A., Gottschalck, J., Mitchell, K., Meng, C.J., Arsenault, K.,
1008 Cosgrove, B., Radakovich, J., Bosilovich, M. and Entin, J.K.: The global land data assimilation system.
1009 *Bulletin of the American Meteorological society*, 85\(3\), pp.381-394.
1010 <https://doi.org/10.1175/BAMS-85-3-381>, 2004.](https://doi.org/10.1017/S1743921314005535)

1011
1012 Rodriguez-Solano, C.J., Hugentobler, U., Steigenberger, P., Bloßfeld, M. and Fritsche, M.: Reducing the
1013 draconitic errors in GPS geodetic products. *Journal of Geodesy*, 88(6), pp.559-574.
1014 <https://doi.org/10.1007/s00190-014-0704-1>, 2014.
1015
1016 Rui, H., Beaudoin, H. and Loeser, C.: README document for NASA GLDAS version 2 data products.
1017 Goddard Earth Sciences Data and Information Services Center (GES DISC): Greenbelt, MD, USA, 2018.
1018
1019 Santamaria-Gomez, A., Gravelle, M., Collilieux, X., Guichard, M., Míguez, B.M., Tiphaneau, P. and
1020 Wöppelmann, G.: Mitigating the effects of vertical land displacement in tide gauge records using a state-
1021 of-the-art GPS velocity field. *Global and Planetary Change*, 98, pp.6-17.
1022 <https://doi.org/10.1016/j.gloplacha.2012.07.007>, 2012.
1023
1024 Schwarz, G.: Estimating the dimension of a model. *Annals of statistics*, 6(2), pp.461-464.
1025 <https://doi.org/10.1214/aos/1176344136>, 1978.
1026
1027 Serpelloni, E., Faccenna, C., Spada, G., Dong, D. and Williams, S.D.: Vertical GPS ground motion rates
1028 in the Euro-Mediterranean region: New evidence of velocity gradients at different spatial scales along the
1029 Nubia-Eurasia plate boundary. *Journal of Geophysical Research: Solid Earth*, 118(11), pp.6003-6024.
1030 <https://doi.org/10.1002/2013JB010102>, 2013.
1031
1032 Simmons, A., Uppala, S., Dee, D. and Kobayashi, S.: ERA-Interim: New ECMWF reanalysis products
1033 from 1989 onwards. *ECMWF newsletter*, 110, 25-35. <https://doi.org/10.21957/pocnex23c6>, 2007.
1034
1035 Sun, Y., Riva, R. and Ditmar, P.: Optimizing estimates of annual variations and trends in geocenter
1036 motion and J2 from a combination of GRACE data and geophysical models, *J. Geophys. Res. Solid Earth*,
1037 121, <https://doi.org/10.1002/2016JB013073>, 2016.
1038
1039 Tapley, B.D., Watkins, M.M., Flechtner, F., Reigber, C., Bettadpur, S., Rodell, M., Sasgen, I.,
1040 Famiglietti, J.S., Landerer, F.W., Chambers, D.P. and Reager, J.T.: Contributions of GRACE to
1041 understanding climate change. *Nature climate change*, 9(5), pp.358-369.
1042 <https://doi.org/10.1038/s41558-019-0456-2>, 2019.
1043
1044 Thomas, A.C., Reager, J.T., Famiglietti, J.S. and Rodell, M.: A GRACE-based water storage deficit
1045 approach for hydrological drought characterization. *Geophysical Research Letters*, 41(5), pp.1537-1545.
1046 <https://doi.org/10.1002/2014GL059323>, 2014.
1047
1048 Thomas, B.F., Famiglietti, J.S., Landerer, F.W., Wiese, D.N., Molotch, N.P. and Argus, D.F.:
1049 Groundwater drought index: Evaluation of California Central Valley groundwater drought. *Remote*
1050 *Sensing of Environment*, 198, pp.384-392. <https://doi.org/10.1016/j.rse.2017.06.026>, 2017.
1051
1052 Tian, Y. and Shen, Z.K.: Extracting the regional common-mode component of GPS station position time
1053 series from dense continuous network. *Journal of Geophysical Research: Solid Earth*, 121(2), pp.1080-
1054 1096. <https://doi.org/10.1002/2015JB012253>, 2016.

1055
1056 Tregoning, P., Watson, C., Ramillien, G., McQueen, H. and Zhang, J.: Detecting hydrologic deformation
1057 using GRACE and GPS. *Geophysical Research Letters*, 36(15). <https://doi.org/10.1029/2009GL038718>,
1058 2009.
1059
1060 Tsai, V.C.: A model for seasonal changes in GPS positions and seismic wave speeds due to thermoelastic
1061 and hydrologic variations. *Journal of Geophysical Research: Solid Earth*, 116(B4).
1062 <https://doi.org/10.1029/2010JB008156>, 2011.
1063
1064 van Dam, T., Wahr, J. and Lavallée, D.: A comparison of annual vertical crustal displacements from GPS
1065 and Gravity Recovery and Climate Experiment (GRACE) over Europe. *Journal of Geophysical Research:*
1066 *Solid Earth*, 112(B3). <https://doi.org/10.1029/2006JB004335>, 2007.
1067
1068 Van Dam, T., Wahr, J., Milly, P.C.D., Shmakin, A.B., Blewitt, G., Lavallée, D. and Larson, K.M.: Crustal
1069 displacements due to continental water loading. *Geophysical Research Letters*, 28(4), pp.651-654.
1070 <https://doi.org/10.1029/2000GL012120>, 2001.
1071
1072 Velicogna, I., Mohajerani, Y., Landerer, F., Mouginot, J., Noel, B., Rignot, E., Sutterley, T., van den
1073 Broeke, M., van Wessem, M. and Wiese, D.: Continuity of ice sheet mass loss in Greenland and
1074 Antarctica from the GRACE and GRACE Follow-On missions. *Geophysical Research Letters*, 47(8),
1075 p.e2020GL087291. <https://doi.org/10.1029/2020GL087291>, 2020.
1076
1077 [Wahr, J., Molenaar, M. and Bryan, F.: Time variability of the Earth's gravity field: Hydrological](https://doi.org/10.1029/1998JB02844)
1078 [and oceanic effects and their possible detection using GRACE. *Journal of Geophysical*](https://doi.org/10.1029/1998JB02844)
1079 [Research: Solid Earth, 103\(B12\), pp.30205-30229. <https://doi.org/10.1029/98JB02844>, 1998.](https://doi.org/10.1029/1998JB02844)
1080
1081 Wang, H., Xiang, L., Jia, L., Jiang, L., Wang, Z., Hu, B. and Gao, P.: Load Love numbers and Green's
1082 functions for elastic Earth models PREM, iasp91, ak135, and modified models with refined crustal
1083 structure from Crust 2.0. *Computers & Geosciences*, 49, pp.190-199.
1084 <https://doi.org/10.1016/j.cageo.2012.06.022>, 2012.
1085
1086 Watkins, M.M., Wiese, D.N., Yuan, D.N., Boening, C. and Landerer, F.W.: Improved methods for
1087 observing Earth's time variable mass distribution with GRACE using spherical cap mascons. *Journal of*
1088 *Geophysical Research: Solid Earth*, 120(4), pp.2648-2671. <https://doi.org/10.1002/2014JB011547>, 2015.
1089
1090 Wdowinski, S., Bock, Y., Zhang, J., Fang, P. and Genrich, J.: Southern California permanent GPS
1091 geodetic array: Spatial filtering of daily positions for estimating coseismic and postseismic displacements
1092 induced by the 1992 Landers earthquake. *Journal of Geophysical Research: Solid Earth*, 102(B8),
1093 pp.18057-18070. <https://doi.org/10.1029/97JB01378>, 1997.
1094
1095 Wessel, P., Luis, J.F., Uieda, L., Scharroo, R., Wobbe, F., Smith, W.H. and Tian, D.: The generic
1096 mapping tools version 6. *Geochemistry, Geophysics, Geosystems*, 20(11), pp.5556-5564.
1097 <https://doi.org/10.1029/2019GC008515>, 2019.
1098

1099 Wiese, D.N., Bienstock, B., Blackwood, C., Chrono, J., Loomis, B.D., Sauber, J., Rodell, M., Baize, R.,
1100 Bearden, D., Case, K. and Horner, S.: The mass change designated observable study: overview and
1101 results. *Earth and Space Science*, 9(8), p.e2022EA002311. <https://doi.org/10.1029/2022EA002311>, 2022.
1102
1103 Wiese, D.N., Landerer, F.W. and Watkins, M.M.: Quantifying and reducing leakage errors in the JPL
1104 RL05M GRACE mascon solution. *Water Resources Research*, 52(9), pp.7490-7502.
1105 <https://doi.org/10.1002/2016WR019344>, 2016.
1106
1107 Williams, S.D.: CATS: GPS coordinate time series analysis software. *GPS solutions*, 12(2), pp.147-153.
1108 <https://doi.org/10.1007/s10291-007-0086-4>, 2008.
1109
1110 Williams, S.D., Bock, Y., Fang, P., Jamason, P., Nikolaidis, R.M., Prawirodirdjo, L., Miller, M. and
1111 Johnson, D.J.: Error analysis of continuous GPS position time series. *Journal of Geophysical Research:*
1112 *Solid Earth*, 109(B3). <https://doi.org/10.1029/2003JB002741>, 2004.
1113
1114 Wu, S., Nie, G., Liu, J., Wang, K., Xue, C., Wang, J., Li, H., Peng, F. and Ren, X.: A sub-regional
1115 extraction method of common mode components from IGS and CMONOC stations in China. *Remote*
1116 *Sensing*, 11(11), p.1389. <https://doi.org/10.3390/rs11111389>, 2019.
1117
1118 Yin, G., Forman, B.A., Loomis, B.D. and Luthcke, S.B.: Comparison of Vertical Surface Deformation
1119 Estimates Derived From Space-Based Gravimetry, Ground-Based GPS, and Model-Based Hydrologic
1120 Loading Over Snow-Dominated Watersheds in the United States. *Journal of Geophysical Research: Solid*
1121 *Earth*, 125(8), p.e2020JB01943. <https://doi.org/10.1029/2020JB019432>, 2020.